Topological Origin of Andreev Flatland in UTe$_2$:
Implication for Josephson STM Measurements

Jushin Tei,[1,*] Takeshi Mizushima,[1] and Satoshi Fujimoto[1,2,3,4]

[1]*Department of Materials Engineering Science, The University of Osaka, Toyonaka 560-8531, Japan*
[2]*Center for Quantum Information and Quantum Biology,*
The University of Osaka, Toyonaka 560-8531, Japan
[3]*Center for Spintronics Research Network, Graduate School of Engineering Science, The University of Osaka*
[4]*Division of Spintronics Research Network, Institute for Open and*
Transdisciplinary Research Initiatives, The University of Osaka
(Dated: April 24, 2025)

We propose the surface of topological superconductors as a platform for realizing two-dimensional flat bands, where electron interactions play a crucial role. The surface flat bands originate from topological features supported by two key mechanisms: (1) a trivial Chern number prevents the zero-energy states from merging into the continuum of the bulk spectrum, thereby ensuring their confinement within the superconducting gap; and (2) weak spin conservation allows the gap function to exhibit phase winding. As a consequence, the surface exhibits a remarkably high density of states at nearly zero energy. Such surface states are likely to be realized in the candidate topological superconductor UTe$_2$. Our results provide important insights into the interpretation of recent Josephson STM experiments on UTe$_2$.

Introduction.—Two-dimensional (2D) flat-band systems have garnered significant attention as ideal platforms for exploring strong correlation effects [1–3]. Moiré systems such as twisted multilayer graphene and transition metal dichalcogenides, provide prominent examples in which electron correlations within narrow bands outweigh kinetic energy, giving rise to unconventional superconductivity, correlated insulating phases, and various topological phenomena [1, 2, 4–7]. In this Letter, we propose that topologically originated flat bands can emerge on specific surfaces of point-nodal spin-triplet superconductors, and discuss their potential realization in the candidate spin-triplet superconductor UTe$_2$ [8–10].

On the surface of a topological superconductor, zero-energy states—known as surface Andreev bound states—emerge as a hallmark of its topological nature [11–17]. This topological character is fundamentally linked to the odd-parity symmetry of the gap function, which satisfies the Andreev condition $\Delta(\boldsymbol{k}) = -\Delta(-\boldsymbol{k})$. Consequently, observing surface Andreev bound states is a powerful probe for identifying the pairing symmetry of unconventional superconductors.

The presence of surface Andreev bound states directly influences the surface density of states (sDOS). However, such states do not necessarily lead to a distinctive zero-bias peak in the sDOS. For instance, in point-nodal superconductors, zero-energy flat bands connecting the point nodes—also known as Fermi arcs—can emerge on the surface, yet they do not produce a zero-bias peak in the sDOS [18, 19]. Notable exceptions include high-$T_{\rm c}$ cuprate superconductors [12, 20–22] and odd-parity superconductors derived from topological insulators [23–26]. In the former, the combination of bulk line nodes in $d_{x^2-y^2}$-wave pairing and the formation of Andreev bound
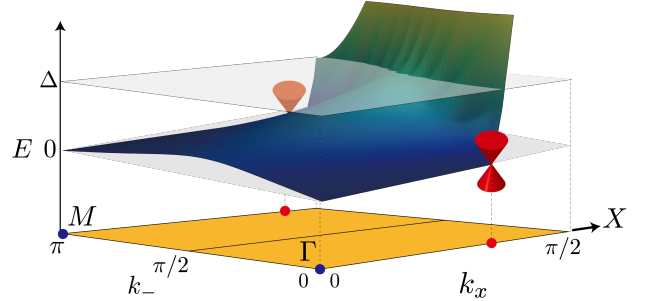
FIG. 1. Quasiparticle energy bands on the (011) plane for the superconducting B_{3u} state. A substantial number of Andreev bound states form a 2D flat-band structure—referred to as the "Andreev flatland"—within the superconducting gap Δ. The red cones indicate the point nodes of the bulk superconducting gap.

states on the (110) surface lead to 2D flat bands, resulting in a sharp zero-bias peak in the sDOS. In the latter, the dispersion of the gapless surface Andreev bound states is intertwined with that of the surface Dirac cone inherited from the parent topological insulator, forming a smooth spectral connection between them. This continuous linkage enhances the sDOS at zero energy. Since UTe$_2$ is believed to be either a point nodal or a fully gapped superconductor, and its normal state is topologically trivial, these mechanisms are not directly applicable.

In this Letter, we reveal the topological origin of surface Andreev bound states that form a 2D flat-band structure extending over the surface Brillouin zone (BZ), which we refer to as the "Andreev flatland". As a concrete example, we examine the (011) surface of the superconducting B_{3u} state, which is one of the

possible pairing states proposed for the topological superconductor candidate UTe$_2$. The formation of the Andreev flatland relies on two key factors: the cylindrical Fermi surface and the orientation of the (011) surface. The resulting surface states are protected by two distinct topological mechanisms: (1) Nontrivial Berry phases are defined at multiple high-symmetry points in the (011) surface BZ, and the corresponding zero-energy states remain confined within the superconducting gap due to the triviality of the mirror Chern number. This scenario can be viewed as a special case of the Thouless pump mechanism, where a nontrivial phase winding characterized by a Chern number guarantees the emergence of surface states that connect bulk bands with different topological characters [27–29]. (2) Weak spin conservation intrinsic to the B_{3u} state, allows the gap function to exhibit nontrivial phase winding, leading to additional surface states protected by a 1D winding number. Owing to these mechanisms, the Andreev flatland gives rise to a pronounced zero-bias peak in the sDOS.

Scanning tunneling microscopy (STM) and spectroscopy (STS) are powerful techniques for probing the sDOS. Recent advances in Josephson STM, which features a superconducting tip, have enabled high-resolution spectroscopy of low-energy excitations on superconducting surfaces [30–34]. Josephson STM has recently been applied to UTe$_2$, where the tunneling current is primarily governed by Andreev reflection processes [35–37]. In Andreev spectroscopy, electrons and holes from UTe$_2$ tunnel into the s-wave superconductor tip and form Cooper pairs, and vice versa. However, interpreting the differential conductance (dI/dV) spectra in Andreev spectroscopy remains challenging, especially in the context of unconventional superconductivity. In this work, we analyze the tunneling current in a point-contact geometry between UTe$_2$ and an s-wave superconducting tip, focusing on the role of Andreev reflections. In the low-bias regime, the dI/dV characteristics are directly determined by the convolution of the sDOS of the superconducting sample. Finally, by comparing our theoretical results with recent STM/STS experiments using an Nb superconducting tip [36, 37], we discuss the possible realization of the Andreev flatland on the surface of UTe$_2$.

Minimal Model.— We begin by describing a minimal model Hamiltonian for UTe$_2$. This compound crystallizes in a body-centered orthorhombic lattice with the point group D_{2h}. The geometry of the Fermi surface plays a crucial role in realizing topological superconductivity. Recent de Haas-van Alphen experiments have observed Fermi surfaces, which consist of two cylindrical sheets— one electron-like and one hole-like—extending along the k_z-direction [38, 39]. To capture the essential features, we consider a tight-binding model on a simple orthogonal lattice with a Kramers-degenerate spin degree of freedom.
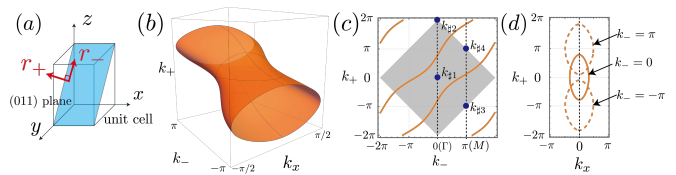
FIG. 2. (a) A naturally cleavable (011) plane. (b) Cylindrical Fermi surface elongated along the k_z-axis, plotted in the rotated coordinate system (k_x, k_+, k_-), where the $k_y k_z$-plane is rotated by $\pi/4$ around the k_x-axis. (c) Plot of the $k_x = 0$ plane in the first Brillouin zone (shaded area), with the Fermi surface shown as orange curves. $k_{\sharp i}$ ($i = 1 \sim 4$) denotes the time-reversal-invariant momenta (TRIMs). Nontrivial Berry phases can be defined along one-dimensional paths in $k_+ \in [-2\pi, 2\pi]$, centered at $\Gamma = (k_x = 0, k_m = 0)$ and $M = (k_x = 0, k_m = \pi)$. Each path connects a pair of TRIMs lying along the k_+ direction. (d) Fermi surface plots at $k_m = 0$ (solid curves) and $k_m = \pm\pi$ (dashed curves).

The normal-state Hamiltonian is given by $H_{\mathrm{N}}(\boldsymbol{k}) = 2t_1 \cos k_x + 2t_2 \cos k_y + 2t_3 \cos k_z - \mu$. To reproduce the cylindrical Fermi surface shown in Fig. 2(b), we set the parameters as $t_1 = -1.0$, $t_2 = -1.0$, $t_3 = 0.25$, and $\mu = -2.5$. Although this minimal model is adopted for clarity, we have verified that our main results remain robust against moderate variations in the parameters, as well as in more realistic models that incorporate orbital degrees of freedom, detailed Fermi surface topology, and staggered Rashba spin-orbit coupling (SOC) arising from local inversion symmetry breaking [40]. As demonstrated in the following, the cylindrical geometry of the Fermi surface plays a particularly crucial role.

The gap function for spin-triplet Cooper pairs is described by the d-vector: $\hat{\Delta}(\boldsymbol{k}) = \boldsymbol{d}(\boldsymbol{k}) \cdot \boldsymbol{\sigma} i\sigma_y$. The point group D_{2h} allows four odd-parity irreducible representations:

$$\boldsymbol{d}_{A_u}(\boldsymbol{k}) = (C_x \sin k_x, C_y \sin k_y, C_z \sin k_z)^{\mathrm{T}}, \tag{1}$$

$$\boldsymbol{d}_{B_{1u}}(\boldsymbol{k}) = (C_x \sin k_y, C_y \sin k_x, C_z \sin k_x \sin k_y \sin k_z)^{\mathrm{T}}, \tag{2}$$

$$\boldsymbol{d}_{B_{2u}}(\boldsymbol{k}) = (C_x \sin k_z, C_y \sin k_x \sin k_y \sin k_z, C_z \sin k_x)^{\mathrm{T}}, \tag{3}$$

$$\boldsymbol{d}_{B_{3u}}(\boldsymbol{k}) = (C_x \sin k_x \sin k_y \sin k_z, C_y \sin k_z, C_z \sin k_y)^{\mathrm{T}}, \tag{4}$$

where $\boldsymbol{a}^{\mathrm{T}}$ denotes the transpose of a vector $\boldsymbol{a}$. The A_u state corresponds to a fully gapped superconductor. The B_{1u} state is also fully gapped, due to the absence of a Fermi surface along the k_z axis. In contrast, the B_{2u} and B_{3u} states are Dirac superconductors with point nodes along the k_x and k_y axes, respectively.

In this study, we focus on the (011) surface as illustrated in Fig. 2(a). To facilitate the analysis, we introduce a rotated coordinate system (x, r_+, r_-), where the yz-plane is rotated by $\pi/4$ around the x-axis. The corresponding rotated momenta are defined as $k_+ = k_y + k_z$ and $k_- = -k_y + k_z$. Since the (011) surface is perpendicular to the r_+ direction; the momenta k_x
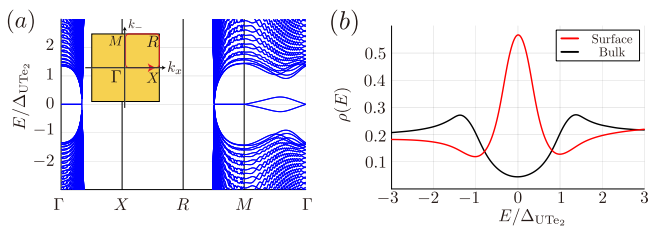
FIG. 3. (a) Quasiparticle energy bands for the B_{3u} state with the parameters $C_x = 0.0$, $C_y = 0.05$, and $C_z = 0.05$. Δ_{UTe_2} is set to 0.05. The inset shows the momentum path in the surface BZ depicted in the main panel. A zero-energy flat band appears along the $\Gamma - X$ and $R - M$ lines, while a nearly zero-energy flat band emerges along the $M - \Gamma$ line. (b) Density of states for surface (red) and bulk (black). The Andreev flatland exhibits a prominent zero-energy peak.

and k_- are conserved. Figures 2(b-d) show the BZ in the rotated coordinate frame.

Flatland and its Topological Origin.— In this section, we mainly consider the B_{3u} state with the parameters set to $C_x = 0$, $C_y = 0.05$, and $C_z = 0.05$. We diagonalize a slab system with the (011) surfaces. Figure 3(a) shows the quasiparticle energy spectrum along the symmetric path $\Gamma(0,0) - X(\pi,0) - R(\pi,\pi) - M(0,\pi) - \Gamma$, where (k_x, k_m) represents the momenta in the surface BZ. Remarkably, we observe the emergence of a zero-energy flat band along the $\Gamma - X$ and $R - M$ lines, as well as an almost flat band near zero energy along the $M - \Gamma$ line. These surface Andreev bound states extend across the 2D surface Brillouin zone, forming a nearly flat-band structure, referred to as the Andreev flatland, as illustrated in Fig. 1.

We compute the sDOS using the recursive Green's function method [41, 42]. The smearing factor δ, which corresponds to the resolution of the energy, is set to $\delta = 0.2\Delta_{\text{UTe}_2}$, where $\Delta_{\text{UTe}_2} = 0.05$. Note that Δ_{UTe_2} serves as a prefactor in the d-vector, and does not represent actual superconducting gap magnitude. As shown in Fig. 3(b), a pronounced zero-energy peak in the sDOS appears as a result of the Andreev flatland. In the supplementary material, we also present the quasiparticle energy bands and sDOS for the A_u, B_{1u}, and B_{2u} states, which exhibit surface flat bands along the $M - \Gamma$ line, but no sharp zero-energy peak is observed in these states [40]. We emphasize that the presence of flatness along a 1D line only, which may arise from gap symmetry, does not necessarily lead to a zero-energy peak in the sDOS.

Indeed, the 2D flat band shown in Fig. 3(a) has a topological origin. To clarify this point, we first discuss the nearly zero-energy flat band along the $M - \Gamma$ direction, which emerges as a direct consequence of the cylindrical Fermi surface geometry. The non-chiral B_{3u} superconducting state belongs to class DIII in the Altland-Zirnbauer classification [43]. Since the B_{3u} state is a nodal superconductor with point nodes along the

k_x-axis, a 3D topological invariant is not well-defined. Instead, its topological properties must be characterized in terms of lower-dimensional topological invariants or crystalline symmetries.

Among these, a central role is played by a Berry phase, a $\mathbb{Z}_2$ topological invariant defined along the closed loops in momentum space. Specifically, we consider loops along $k_+ \in [-2\pi, 2\pi]$ at two high-symmetry momentum points—the Γ and M points—as illustrated by the dashed lines in Fig. 2(c) [44]. The Berry phase along each loop is determined by the parity of the number of Fermi surfaces that intersect the loop between two time-reversal-invariant momenta, denoted $k_{\sharp i}$. When the number of intersecting Fermi surfaces is odd (even), the Berry phase is nontrivial (trivial) [13, 14]. As a consequence, topologically protected zero-energy states appear at both the Γ and M points. Notably, this type of topological protection is unique to the (011) surface. On high-symmetry surfaces such as (100), (010), and (001), an analogous Berry phase structure does not arise.

At the same time, the (011) surface preserves mirror reflection symmetry with respect to the yz plane. On the mirror-invariant plane $k_x = 0$, the Hamiltonian can be block-diagonalized according to the eigenvalues of the mirror symmetry operator. As a result, a mirror Chern number can be defined for each mirror subsector. However, this mirror Chern number vanishes due to the quasi-1D nature of the cylindrical Fermi surface on the $k_x = 0$ plane. Consequently, the zero-energy states at the M and Γ points cannot be connected to the continuum of bulk spectrum in the absence of a Thouless pump. This implies that the nearly zero-energy flat band along the $M - \Gamma$ line is topologically protected by the triviality of the mirror Chern number.

The origin of another set of zero-energy flat bands along the $\Gamma - X$ and $R - M$ lines lies in a weak spin conservation intrinsic to the B_{3u} state. Although these states are not topologically protected in the strict sense, the presence of in-gap states (not necessarily at zero energy) can still be robust, as we will discuss in the next section. When the d_x component vanishes ($C_x = 0$), the gap function can be diagonalized by a spin rotation, yielding $\hat{\Delta} = \text{diag}(d_z + id_y, -d_z + id_y)$. This form reveals spin conservation, where the spin quantization axis is along the x-direction. If we consider only up-spin Cooper pairs, the gap function reduces to

$$\Delta_{\uparrow\uparrow} \propto e^{i\pi/4} \sin\frac{k_+}{2} \cos\frac{k_-}{2} - e^{-i\pi/4} \cos\frac{k_+}{2} \sin\frac{k_-}{2}. \quad (5)$$

Within the up-spin subspace, we can define a winding number $w(k_x, k_m)$ associated with the chiral symmetry along the 1D path $k_+ \in [-2\pi, 2\pi]$ as a function of k_x and k_m. This winding number can be evaluated using Fermi
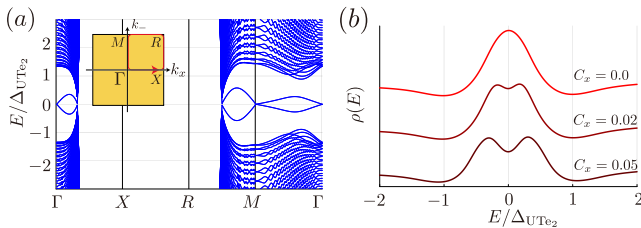
FIG. 4. (a) Quasiparticle energy bands for the B_{3u} state with parameters $C_x = 0.05$, $C_y = 0.05$, and $C_z = 0.05$. $\Delta_{\mathrm{UTe_2}}$ is set to 0.05. The d_x component breaks spin conservation, resulting in a gap opening in the zero-energy flat band. (b) Surface density of states as a function of C_x.

surface formula [15]

$$w = \frac{1}{2} \sum_{E_N(k_+)=0} \mathrm{sgn}[\Delta_{\uparrow\uparrow}] \mathrm{sgn}[\partial_{k_+} E_N]. \tag{6}$$

As shown in Fig. 2(d), along the $\Gamma - X$ line ($k_m = 0$), the Fermi surface is symmetric concerning k_+, and the gap function $\Delta_{\uparrow\uparrow} \propto \sin(k_+/2)$ is an odd function of k_+. Consequently, the winding number is $w = 1$ whenever the 1D k_+ path crosses the Fermi surface. Similarly, the winding number is $w = 1$ along the $R - M$.

These two types of topologically protected Andreev bound states—those stabilized by the triviality of the mirror Chern number and those protected by the winding number associated with accidental spin degeneracy—jointly contribute to the formation of the 2D Andreev flatland.

Spin Flipping Effect Due to the d_x Component.— As discussed in the previous section, the zero-energy flat bands along the $\Gamma - X$ and $R - M$ lines arise from spin conservation resulting from the absence of the d_x component. The presence of a d_x component violates spin conservation, leading to spin flip. Here, we examine the stability of the Andreev flatland against a finite d_x component. Figure 4(a) shows the quasiparticle energy spectrum for the B_{3u} state with pairing parameters set to $C_x = 0.05$, $C_y = 0.05$, and $C_z = 0.05$. The zero-energy flat bands that previously existed in the $\Gamma - X$ and $R - M$ lines in Fig. 3(a) are now gapped out. As a result of spin flipping, the sDOS exhibits a maximum at finite energy, corresponding to van Hove singularities of surface states, as shown in Fig. 4(b). Nevertheless, although the flat bands are lifted from zero energy, a substantial number of surface states remain within the superconducting gap. In this sense, weak spin conservation along the x-direction allows Andreev flatland to remain robust. The extent to which these states stay close to zero energy depends on the specific model. However, as long as the d_x component remains sufficiently small—comparable to the energy resolution—a zero-energy peak in the sDOS continues to be present.

Effect of Spin-Orbit Coupling.— Although our starting
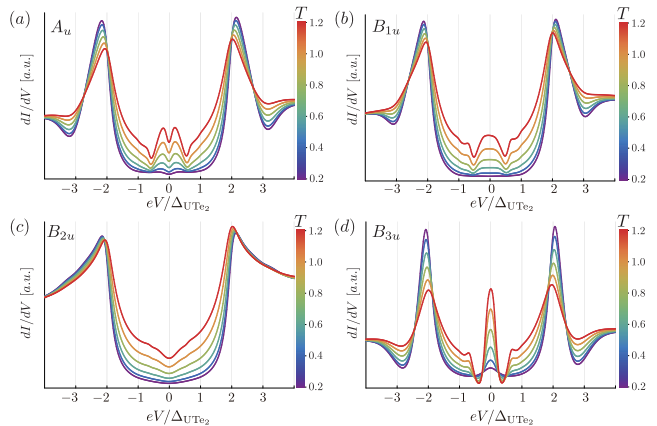
FIG. 5. Normalized differential conductance (dI/dV) of a point contact between UTe$_2$ and an s-wave superconductor. The superconducting state in UTe$_2$ corresponds to the (a) A_u, (b) B_{1u}, (c) B_{2u}, and (d) B_{3u} representations, respectively. The s-wave superconducting gap is set to $\Delta_s = 2\Delta_{\mathrm{UTe_2}}$. The color bar represents the amplitude of tunneling matrix element T. A prominent zero-bias peak, comparable in height to the coherence peak at $eV = \Delta_s$, emerges due to the presence of Andreev flatland in the B_{3u} case.

model assumes Kramers spin degeneracy, the effects of atomic SOC and staggered Rashba SOC—arising from local inversion symmetry breaking at the uranium sites—are effectively taken into account. Therefore, the Andreev flatland remains robust even in the presence of SOC. In the Supplemental Material [40], we explicitly demonstrate that the Andreev flatland persists in a two-orbital model that includes staggered Rashba SOC.

Andreev Current Spectroscopy in UTe$_2$.— UTe$_2$ is widely recognized as a spin-triplet p-wave superconductor, as suggested by its distinctive properties: exceptionally high upper critical fields [8–10], multiple superconducting phases induced by pressure and magnetic fields [45–51], and a minimal reduction in the NMR Knight shift [52, 53]. A central topic is the nature of its pairing symmetry, which governs low-energy excitations and topological properties. Various experimental studies [52–59] and theoretical works [60–68] have been conducted to elucidate the pairing symmetry. Despite these extensive efforts, the issue remains unresolved. Recently, STM/STS experiments were performed on the naturally cleavable (011) surface of UTe$_2$, using both a normal-metal tip [35, 54, 69–72] and a superconducting tip [35–37]. In particular, the use of superconducting tips has enabled high-resolution measurements of low-energy features. Remarkably, a sharp zero-bias peak was observed, comparable in magnitude to the coherence peaks of the superconducting tip [36, 37].

To investigate recent STM/STS experiments using an s-wave superconducting tip, we compute the tunneling current across a point contact between an s-wave

superconductor and each of the possible irreducible representations proposed for UTe$_2$. The total Hamiltonian is given by $\mathcal{H} = \mathcal{H}_{\text{UTe}_2} + \mathcal{H}_{s-\text{wave}} + \mathcal{H}_T$, where the tunneling term is expressed as $\mathcal{H}_T = T\sum_{k,q} c_k^\dagger c_q + \text{h.c.}$. Here, T represents the tunneling matrix, and c_k (c_q) denotes the electron annihilation operator for UTe$_2$ (the s-wave superconducting tip). Since tunneling occurs through a point contact, momentum does not conserve, and the tunneling matrix is taken to be momentum-independent. The tunneling current, defined as $I(V) = e\langle \dot{N}_{\text{UTe}_2}\rangle$, is evaluated by perturbation theory using Keldysh Green's function formalism [73]. The details are described in the Supplementary Material [40].

The tunneling current consists of three contributions. The first is the single-particle tunneling, which vanishes at low bias ($eV < \Delta_s$) due to the absence of available quasiparticle states in the s-wave superconducting tip. The second contribution arises from Cooper pair tunneling, which is either absent or highly suppressed due to the spin-space orthogonality between spin-triplet and spin-singlet superconductors [74, 75]. The third and dominant contribution is Andreev tunneling between the surface Andreev bound states of the topological superconductor and the Cooper pairs of an s-wave superconductor. In this process, electrons and holes in the surface Andreev bound states of the topological superconductor are converted into Cooper pairs in the s-wave superconductor and vice versa.

We now present the normalized differential conductance, dI/dV, calculated using Eq. (S22) in Supplemental Material [40], which incorporates tunneling processes to all orders, as shown in Fig. 5. In these calculations, the s-wave superconducting gap is set to $\Delta_s = 2\Delta_{\text{UTe}_2}$. Remarkably, we observe an exceptionally sharp zero-bias peak in the B_{3u} state, with a magnitude comparable to that of the coherence peaks of the s-wave superconducting tip. This dI/dV spectrum is in excellent agreement with recent experimental observations [36, 37]. To gain qualitative insight into the behavior near zero bias, we derive the expression for the Andreev tunneling current in the weak-coupling limit:

$$I(V) = \frac{4e}{\hbar} T^4 \pi^3 N_s^2 \int_0^{2eV} dE\; \rho(E - 2eV)\rho(E), \quad (7)$$

where N_s represents the normal-state density of state at the Fermi level of the s-wave superconducting tip, and $\rho(E)$ denotes the sDOS in the superconducting sample. Notably, the Andreev tunneling current originates from a fourth-order perturbation process in the tunnel Hamiltonian as reflected in T^4 dependence, and it is independent of the s-wave superconducting gap Δ_s. Consequently, the appearance of a zero-bias peak serves as a direct signature of the Andreev flatland. Importantly, such a pronounced zero-bias peak in the (011) surface is unique to the B_{3u} state. Thus, these results support the realization of the B_{3u} pairing state

in UTe$_2$. However, it should be noted that no zero-bias peak has been reported in STM/STS experiments using normal-metal tips [36, 37], even though the presence of the Andreev flatland is expected to produce a similar signature regardless of the tip type. This discrepancy underscores the need for a more careful and comprehensive examination of the origin of the zero-bias peak and underlying pairing symmetry in UTe$_2$.

Conclusion.— Motivated by the observation of a pronounced zero-bias peak in STM/STS experiments using an Nb superconducting tip, we have investigated Andreev bound states on the (011) surface of UTe$_2$. In the superconducting B_{3u} state, an Andreev flatland—a nearly flat band state within the superconducting gap—emerges, giving rise to a prominent zero-energy peak in sDOS. The experimental observation of a zero-bias peak in UTe$_2$ strongly suggests the presence of the Andreev flatland and, consequently, supports the realization of the B_{3u} pairing state. However, the absence of a zero-bias peak in experiments using a normal-metal tip calls for further theoretical and experimental studies.

Although our discussion has focused on UTe$_2$, the underlying model is broadly applicable. The formation of the Andreev flatland is primarily attributed to the cylindrical geometry of the Fermi surface. In particular, the geometry allows for multiple Berry phases to arise on specific surfaces. At the same time, the trivial mirror Chern number—also a consequence of the cylindrical geometry—prevents the zero-energy states, protected by the Berry phases, from merging into the continuum of the bulk spectrum. Importantly, this mechanism for in-gap state formation is not unique to the B_{3u} state. Even in the fully gapped A_u state, although a zero-bias peak does not appear in the sDOS, isolated in-gap states are still present on the (011) surface. Similar features can also arise in the B_{1u} and B_{2u}, depending on the surface orientation. A natural direction for future work is to generalize these results to other Fermi surface geometries and topological symmetry classes. Furthermore, strong correlation effects in flat bands on topological superconducting surfaces present a particularly intriguing avenue for further exploration. The surface of a topological superconductor is not a purely 2D system; rather, it constitutes an anomalous surface—one that inherits the Bogoliubov quasiparticles. Interaction-induced gapping without symmetry breaking could potentially give rise to new classes of topologically ordered phases, distinct from those realized in purely 2D electron systems [76].

————————

* tei@blade.mp.es.osaka-u.ac.jp

[1] L. Balents, C. R. Dean, D. K. Efetov, and A. F. Young, Superconductivity and strong correlations in moiré flat bands, Nat. Phys. **16**, 725 (2020).

[2] E. Y. Andrei and A. H. MacDonald, Graphene bilayers with a twist, Nat. Mater. **19**, 1265 (2020).

[3] P. Törmä, S. Peotta, and B. A. Bernevig, Superconductivity, superfluidity and quantum geometry in twisted multilayer systems, Nat. Rev. Phys. **4**, 528 (2022).

[4] Y. Cao, V. Fatemi, A. Demir, S. Fang, S. L. Tomarken, J. Y. Luo, J. D. Sanchez-Yamagishi, K. Watanabe, T. Taniguchi, E. Kaxiras, *et al.*, Correlated insulator behaviour at half-filling in magic-angle graphene superlattices, Nature **556**, 80 (2018).

[5] Y. Cao, V. Fatemi, S. Fang, K. Watanabe, T. Taniguchi, E. Kaxiras, and P. Jarillo-Herrero, Unconventional superconductivity in magic-angle graphene superlattices, Nature **556**, 43 (2018).

[6] A. Banerjee, Z. Hao, M. Kreidel, P. Ledwith, I. Phinney, J. M. Park, A. Zimmerman, M. E. Wesson, K. Watanabe, T. Taniguchi, *et al.*, Superfluid stiffness of twisted trilayer graphene superconductors, Nature **638**, 93 (2025).

[7] M. Tanaka, J. Î.-j. Wang, T. H. Dinh, D. Rodan-Legrain, S. Zaman, M. Hays, A. Almanakly, B. Kannan, D. K. Kim, B. M. Niedzielski, *et al.*, Superfluid stiffness of magic-angle twisted bilayer graphene, Nature **638**, 99 (2025).

[8] S. Ran, C. Eckberg, Q.-P. Ding, Y. Furukawa, T. Metz, S. R. Saha, I.-L. Liu, M. Zic, H. Kim, J. Paglione, and N. P. Butch, Nearly Ferromagnetic Spin-Triplet Superconductivity, Science **365**, 684 (2019).

[9] D. Aoki, A. Nakamura, F. Honda, D. Li, Y. Homma, Y. Shimizu, Y. J. Sato, G. Knebel, J.-P. Brison, A. Pourret, D. Braithwaite, G. Lapertot, Q. Niu, M. Vališka, H. Harima, and J. Flouquet, Unconventional Superconductivity in Heavy Fermion UTe$_2$, J. Phys. Soc. Jpn. **88**, 043702 (2019).

[10] D. Aoki, J.-P. Brison, J. Flouquet, K. Ishida, G. Knebel, Y. Tokunaga, and Y. Yanase, Unconventional Superconductivity in UTe$_2$, J. Phys. Condens. Matter **34**, 243002 (2022).

[11] C.-R. Hu, Midgap surface states as a novel signature for d_{xa}^2-x_b^2-wave superconductivity, Phys. Rev. Lett. **72**, 1526 (1994).

[12] S. Kashiwaya and Y. Tanaka, Tunnelling effects on surface bound states inunconventional superconductors, Rep. Prog. Phys. **63**, 1641 (2000).

[13] M. Sato, Topological properties of spin-triplet superconductors and fermi surface topology in the normal state, Phys. Rev. B **79**, 214526 (2009).

[14] M. Sato, Topological odd-parity superconductors, Phys. Rev. B **81**, 220504 (2010).

[15] M. Sato, Y. Tanaka, K. Yada, and T. Yokoyama, Topology of andreev bound states with flat dispersion, Phys. Rev. B **83**, 224511 (2011).

[16] J. Alicea, New directions in the pursuit of Majorana fermions in solid state systems, Rep. Prog. Phys. **75**, 076501 (2012).

[17] M. Sato and S. Fujimoto, Majorana fermions and topology in superconductors, J. Phys. Soc. Jpn. **85**, 072001 (2016).

[18] S. A. Yang, H. Pan, and F. Zhang, Dirac and weyl superconductors in three dimensions, Phys. Rev. Lett. **113**, 046401 (2014).

[19] A. P. Schnyder and P. M. R. Brydon, Topological surface states in nodal superconductors, J. Phys. Condens. Matter **27**, 243201 (2015).

[20] S. Kashiwaya, Y. Tanaka, M. Koyanagi, H. Takashima, and K. Kajimura, Origin of zero-bias conductance peaks in high-T_c superconductors, Phys. Rev. B **51**, 1350 (1995).

[21] J. Y. T. Wei, N.-C. Yeh, D. F. Garrigus, and M. Strasik, Directional Tunneling and Andreev Reflection on YBa$_2$Cu$_3$O$_{7-\delta}$ Single Crystals: Predominance of d-Wave Pairing Symmetry Verified with the Generalized Blonder, Tinkham, and Klapwijk Theory, Phys. Rev. Lett. **81**, 2542 (1998).

[22] I. Iguchi, W. Wang, M. Yamazaki, Y. Tanaka, and S. Kashiwaya, Angle-resolved Andreev bound states in anisotropic d-wave high-T_c YBa$_2$Cu$_3$O$_{7-y}$ superconductors, Phys. Rev. B **62**, R6131 (2000).

[23] L. Hao and T. K. Lee, Surface spectral function in the superconducting state of a topological insulator, Phys. Rev. B **83**, 134516 (2011).

[24] T. H. Hsieh and L. Fu, Majorana Fermions and Exotic Surface Andreev Bound States in Topological Superconductors: Application to Cu$_x$Bi$_2$Se$_3$, Phys. Rev. Lett. **108**, 107005 (2012).

[25] A. Yamakage, K. Yada, M. Sato, and Y. Tanaka, Theory of tunneling conductance and surface-state transition in superconducting topological insulators, Phys. Rev. B **85**, 180509 (2012).

[26] S. Sasaki, Z. Ren, A. A. Taskin, K. Segawa, L. Fu, and Y. Ando, Odd-parity pairing and topological superconductivity in a strongly spin-orbit coupled semiconductor, Phys. Rev. Lett. **109**, 217004 (2012).

[27] L. Fu and C. L. Kane, Time reversal polarization and a Z_2 adiabatic spin pump, Phys. Rev. B **74**, 195312 (2006).

[28] L. Fu and C. L. Kane, Topological insulators with inversion symmetry, Phys. Rev. B **76**, 045302 (2007).

[29] D. J. Thouless, Quantization of particle transport, Phys. Rev. B **27**, 6083 (1983).

[30] O. Naaman, W. Teizer, and R. C. Dynes, Fluctuation Dominated Josephson Tunneling with a Scanning Tunneling Microscope, Phys. Rev. Lett. **87**, 097004 (2001).

[31] J. Šmakov, I. Martin, and A. V. Balatsky, Josephson scanning tunneling microscopy, Phys. Rev. B **64**, 212506 (2001).

[32] M. Ternes, W.-D. Schneider, J.-C. Cuevas, C. P. Lutz, C. F. Hirjibehedin, and A. J. Heinrich, Subgap structure in asymmetric superconducting tunnel junctions, Phys. Rev. B **74**, 132501 (2006).

[33] M. T. Randeria, B. E. Feldman, I. K. Drozdov, and A. Yazdani, Scanning Josephson spectroscopy on the atomic scale, Phys. Rev. B **93**, 161115 (2016).

[34] W. Ko, E. F. Dumitrescu, and P. Maksymovych, Statistical detection of Josephson, Andreev, and single

quasiparticle currents in scanning tunneling microscopy, Phys. Rev. Res. **3**, 033248 (2021).

[35] Q. Gu, J. P. Carroll, S. Wang, S. Ran, C. Broyles, H. Siddiquee, N. P. Butch, S. R. Saha, J. Paglione, J. S. Davis, *et al.*, Detection of a pair density wave state in UTe$_2$, Nature **618**, 921 (2023).

[36] Q. Gu, S. Wang, J. P. Carroll, K. Zhussupbekov, C. Broyles, S. Ran, N. P. Butch, S. Saha, J. Paglione, X. Liu, *et al.*, Pair Wavefunction Symmetry in UTe$_2$ from Zero-Energy Surface State Visualization, arXiv:2501.16636 (2025).

[37] S. Wang, K. Zhussupbekov, J. P. Carroll, B. Hu, X. Liu, E. Pangburn, A. Crepieux, C. Pepin, C. Broyles, S. Ran, *et al.*, Imaging Odd-Parity Quasiparticle Interference in the Superconductive Surface State of UTe$_2$, arXiv:2503.17761 (2025).

[38] D. Aoki, H. Sakai, P. Opletal, Y. Tokiwa, J. Ishizuka, Y. Yanase, H. Harima, A. Nakamura, D. Li, Y. Homma, Y. Shimizu, G. Knebel, J. Flouquet, and Y. Haga, First Observation of the de Haas-van Alphen Effect and Fermi Surfaces in the Unconventional Superconductor UTe$_2$, J. Phys. Soc. Jpn. **91**, 083704 (2022).

[39] A. Eaton, T. Weinberger, N. Popiel, Z. Wu, A. Hickey, A. Cabala, J. Pospíšil, J. Prokleška, T. Haidamak, G. Bastien, *et al.*, Quasi-2D Fermi surface in the anomalous superconductor UTe$_2$, Nat. Commun. **15**, 223 (2024).

[40] See Supplement Material at [url] for the topological properties of surface Andreev bound states and the differential conductance spectra (dI/dV) in all possible irreducible representations. It also contains calculations based on a more realistic model of UTe$_2$ and a detailed derivation of the expression for the Andreev tunneling current.

[41] A. Umerski, Closed-form solutions to surface green's functions, Phys. Rev. B **55**, 5266 (1997).

[42] R. Ohashi, J. Tei, Y. Tanaka, T. Mizushima, and S. Fujimoto, Anisotropic paramagnetic response of topological Majorana surface states in the superconductor UTe$_2$, Phys. Rev. B **110**, 174521 (2024).

[43] A. P. Schnyder, S. Ryu, A. Furusaki, and A. W. W. Ludwig, Classification of topological insulators and superconductors in three spatial dimensions, Phys. Rev. B **78**, 195125 (2008).

[44] J. Tei, T. Mizushima, and S. Fujimoto, Possible realization of topological crystalline superconductivity with time-reversal symmetry in UTe$_2$, Phys. Rev. B **107**, 144517 (2023).

[45] S. Ran, I.-L. Liu, Y. S. Eo, D. J. Campbell, P. M. Neves, W. T. Fuhrman, S. R. Saha, C. Eckberg, H. Kim, D. Graf, F. Balakirev, J. Singleton, J. Paglione, and N. P. Butch, Extreme Magnetic Field-Boosted Superconductivity, Nat. Phys. **15**, 1250 (2019).

[46] A. Rosuel, C. Marcenat, G. Knebel, T. Klein, A. Pourret, N. Marquardt, Q. Niu, S. Rousseau, A. Demuer, G. Seyfarth, G. Lapertot, D. Aoki, D. Braithwaite, J. Flouquet, and J. P. Brison, Field-Induced Tuning of the Pairing State in a Superconductor, Phys. Rev. X **13**, 011022 (2023).

[47] Z. Wu, T. I. Weinberger, J. Chen, A. Cabala, D. V. Chichinadze, D. Shaffer, J. Pospíšil, J. Prokleška, T. Haidamak, G. Bastien, V. Sechovský, A. J. Hickey, M. J. Mancera-Ugarte, S. Benjamin, D. E. Graf, Y. Skourski, G. G. Lonzarich, M. Vališka, F. M. Grosche, and A. G. Eaton, Enhanced triplet superconductivity in next-generation ultraclean UTe$_2$, Proc. Natl. Acad. Sci. **121**, e2403067121 (2024).

[48] D. Braithwaite, M. Vališka, G. Knebel, G. Lapertot, J.-P. Brison, A. Pourret, M. E. Zhitomirsky, J. Flouquet, F. Honda, and D. Aoki, Multiple Superconducting Phases in a Nearly Ferromagnetic System, Commun. Phys. **2**, 1 (2019).

[49] D. Aoki, F. Honda, G. Knebel, D. Braithwaite, A. Nakamura, D. Li, Y. Homma, Y. Shimizu, Y. J. Sato, J.-P. Brison, and J. Flouquet, Multiple Superconducting Phases and Unusual Enhancement of the Upper Critical Field in UTe$_2$, J. Phys. Soc. Jpn. **89**, 053705 (2020).

[50] G. Knebel, M. Kimata, M. Vališka, F. Honda, D. Li, D. Braithwaite, G. Lapertot, W. Knafo, A. Pourret, Y. J. Sato, Y. Shimizu, T. Kihara, J.-P. Brison, J. Flouquet, and D. Aoki, Anisotropy of the Upper Critical Field in the Heavy-Fermion Superconductor UTe$_2$ under Pressure, J. Phys. Soc. Jpn. **89**, 053707 (2020).

[51] D. Aoki, M. Kimata, Y. J. Sato, G. Knebel, F. Honda, A. Nakamura, D. Li, Y. Homma, Y. Shimizu, W. Knafo, D. Braithwaite, M. Vališka, A. Pourret, J.-P. Brison, and J. Flouquet, Field-Induced Superconductivity near the Superconducting Critical Pressure in UTe$_2$, J. Phys. Soc. Jpn. **90**, 074705 (2021).

[52] H. Fujibayashi, G. Nakamine, K. Kinjo, S. Kitagawa, K. Ishida, Y. Tokunaga, H. Sakai, S. Kambe, A. Nakamura, Y. Shimizu, Y. Homma, D. Li, F. Honda, and D. Aoki, Superconducting Order Parameter in UTe2 Determined by Knight Shift Measurement, J. Phys. Soc. Jpn. **91**, 043705 (2022).

[53] H. Matsumura, H. Fujibayashi, K. Kinjo, S. Kitagawa, K. Ishida, Y. Tokunaga, H. Sakai, S. Kambe, A. Nakamura, Y. Shimizu, Y. Homma, D. Li, F. Honda, and D. Aoki, Large Reduction in the a-axis Knight Shift on UTe$_2$ with T_c = 2.1 K, J. Phys. Soc. Jpn. **92**, 063701 (2023).

[54] A. Aishwarya, J. May-Mann, A. Raghavan, L. Nie, M. Romanelli, S. Ran, S. R. Saha, J. Paglione, N. P. Butch, E. Fradkin, *et al.*, Magnetic-field-sensitive charge density waves in the superconductor UTe$_2$, Nature **618**, 928 (2023).

[55] S. Lee, A. J. Woods, P. Rosa, S. Thomas, E. Bauer, S.-Z. Lin, and R. Movshovich, Anisotropic field-induced changes in the superconducting order parameter of UTe$_2$, arXiv:2310.04938 (2023).

[56] S. Suetsugu, M. Shimomura, M. Kamimura, T. Asaba, H. Asaeda, Y. Kosuge, Y. Sekino, S. Ikemori, Y. Kasahara, Y. Kohsaka, *et al.*, Fully gapped pairing state in spin-triplet superconductor UTe$_2$, Sci. Adv. **10**, eadk3772 (2024).

[57] I. M. Hayes, T. E. Metz, C. E. Frank, S. R. Saha, N. P. Butch, V. Mishra, P. J. Hirschfeld, and J. Paglione, Robust nodal behavior in the thermal conductivity of superconducting UTe$_2$, arXiv:2402.19353 (2024).

[58] Z. Li, C. M. Moir, N. J. McKee, E. Lee-Wong, R. E. Baumbach, M. B. Maple, and Y. Liu, Observation of odd-parity superconductivity in UTe$_2$, Proc. Natl. Acad. Sci. **122**, e2419734122 (2025).

[59] F. Theuss, A. Shragai, G. Grissonnanche, I. M. Hayes, S. R. Saha, Y. S. Eo, A. Suarez, T. Shishidou, N. P. Butch, J. Paglione, *et al.*, Single-component superconductivity in UTe$_2$ at ambient pressure, Nat.

Phys. **20**, 1124 (2024).

[60] J. Ishizuka and Y. Yanase, Periodic anderson model for magnetism and superconductivity in ute$_2$, Phys. Rev. B **103**, 094504 (2021).

[61] T. Shishidou, H. G. Suh, P. M. R. Brydon, M. Weinert, and D. F. Agterberg, Topological band and superconductivity in UTe$_2$, Phys. Rev. B **103**, 104504 (2021).

[62] A. Kreisel, Y. Quan, and P. J. Hirschfeld, Spin-triplet superconductivity driven by finite-momentum spin fluctuations, Phys. Rev. B **105**, 104507 (2022).

[63] J. J. Yu, Y. Yu, D. F. Agterberg, and S. Raghu, Theory of the low- and high-field superconducting phases of UTe$_2$, Phys. Rev. B **107**, 214510 (2023).

[64] R. Hakuno, K. Nogaki, and Y. Yanase, Magnetism and superconductivity in mixed-dimensional periodic Anderson model for UTe$_2$, Phys. Rev. B **109**, 104509 (2024).

[65] S. Haruna, T. Nomura, and H. Kaneyasu, Possible Unconventional s-Wave Pairing with Point-Node–Like Gap Structure in UTe$_2$, Journal of the Physical Society of Japan **93**, 063701 (2024).

[66] J. Tei, T. Mizushima, and S. Fujimoto, Pairing symmetries of multiple superconducting phases in UTe$_2$: Competition between ferromagnetic and antiferromagnetic fluctuations, Phys. Rev. B **109**, 064516 (2024).

[67] A. Crépieux, E. Pangburn, S. Wang, K. Zhussupbekov, J. P. Carroll, B. Hu, Q. Gu, J. Davis, C. Pépin, and C. Bena, Quasiparticle interference and spectral function of the UTe$_2$ superconductive surface band, arXiv:2503.17762 (2025).

[68] H. Christiansen, M. Geier, B. M. Andersen, and A. Kreisel, Nodal superconducting gap structure and topological surface states of UTe$_2$, arXiv preprint arXiv:2503.11603 (2025).

[69] L. Jiao, S. Howard, S. Ran, Z. Wang, J. O. Rodriguez, M. Sigrist, Z. Wang, N. P. Butch, and V. Madhavan, Chiral superconductivity in heavy-fermion metal UTe$_2$, Nature **579**, 523 (2020).

[70] H. Yoon, Y. S. Eo, J. Park, J. A. Horn, R. G. Dorman, S. R. Saha, I. M. Hayes, I. Takeuchi, P. M. Brydon, and J. Paglione, Probing p-wave superconductivity in UTe$_2$ via point-contact junctions, npj Quantum Mater. **9**, 91 (2024).

[71] N. Sharma, M. Toole, J. McKenzie, F. Cheng, S. M. Thomas, P. F. Rosa, Y.-T. Hsu, and X. Liu, Observation of Persistent Zero Modes and Superconducting Vortex Doublets in UTe$_2$, arXiv:2503.17450 (2025).

[72] R. Yin, Y. Li, Z. Du, D. Yuan, S. Wang, J. Gong, M. Li, Z. Chen, J. Zhang, Y. Wang, *et al.*, Yin-Yang vortex on UTe$_2$ (011) surface, arXiv:2503.21506 (2025).

[73] J. C. Cuevas, A. Martín-Rodero, and A. L. Yeyati, Hamiltonian approach to the transport properties of superconducting quantum point contacts, Phys. Rev. B **54**, 7366 (1996).

[74] V. B. Geshkenbein and A. I. Larkin, The Josephson effect in superconductors with heavy fermions, JETP Lett. **43**, 395 (1986), [Pis'ma Zh. Eksp. Teor. Fiz. **43**, 306 (1986)].

[75] A. Millis, D. Rainer, and J. A. Sauls, Quasiclassical theory of superconductivity near magnetically active interfaces, Phys. Rev. B **38**, 4504 (1988).

[76] X. Chen, F. J. Burnell, A. Vishwanath, and L. Fidkowski, Anomalous symmetry fractionalization and surface topological order, Phys. Rev. X **5**, 041013 (2015).

Supplemental Material for "Topological Origin of Andreev Flatland in UTe$_2$"

Jushin Tei,[1, *] Takeshi Mizushima,[1] and Satoshi Fujimoto[1, 2, 3, 4]

[1]*Department of Materials Engineering Science, The University of Osaka, Toyonaka 560-8531, Japan*
[2]*Center for Quantum Information and Quantum Biology,*
The University of Osaka, Toyonaka 560-8531, Japan
[3]*Center for Spintronics Research Network, Graduate School of Engineering Science, The University of Osaka*
[4]*Division of Spintronics Research Network, Institute for Open and*
Transdisciplinary Research Initiatives, The University of Osaka
(Dated: April 24, 2025)

In this Supplemental Material, we present: (1) the topological invariants and surface Andreev bound states for all possible irreducible representations, including A_u, B_{1u}, and B_{2u}; (2) the differential conductance spectra (dI/dV) for all possible irreducible representation; (3) a demonstration of the presence of the Andreev flatland using a more realistic model of UTe$_2$; and (4) a detailed description for tunneling Hamiltonian approach using Keldysh Green's function formalism.

S1. TOPOLOGICAL INVARIANTS AND SURFACE ANDREEV BOUND STATES

In this section, we present surface Andreev bound states and their topological origins for the A_u, B_{1u}, and B_{2u} states. Figure S1 shows the quasiparticle energy bands and density of states (DOS) for all possible irreducible representations.

The A_u state

On the (011) surface, the topological superconducting properties of the A_u state are similar to those of the B_{3u} state. In particular, since the d_x component vanishes in the $k_x = 0$ plane for both states, the A_u and B_{3u} states differ only in the momentum dependence of their d_y and d_z components. Therefore, although there is some overlap with the discussion of the B_{3u} state in the main text, we will carefully describe the topological superconducting properties of the A_u state in the following.

The fully gapped A_u state is a candidate for a topological superconducting phase. This state preserves time-reversal symmetry and particle-hole symmetry, placing it in class DIII of the Altland-Zirnbauer classification. A 3D winding number can be defined as a strong topological invariant. However, it remains trivial as long as the Fermi surface is a quasi-2D cylindrical shape. Thus, for the A_u state—similar to the B_{3u} state—weak or crystalline topological invariants play a crucial role in the emergence of Andreev bound states.

Figure S1(a) shows the quasiparticle energy bands for the A_u state. Zero-energy states appear at the high-symmetry momentum points Γ and M, originating from a nontrivial Berry phase—similar to those in the B_{3u} state. As understood from the Fermi surface criterion, a nontrivial Berry phase can be defined for all odd-parity irreducible representations. In addition to the Berry phase, a mirror Chern number can be defined since the $k_x = 0$ plane corresponds to the mirror plane of $\mathcal{M}_{yz}$. However, the mirror Chern number vanishes due to the quasi-1D nature of the Fermi surface on the $k_x = 0$ plane. This vanishing mirror Chern number prevents the zero-energy states at the Γ and M points from merging into the continuum of the bulk spectrum. As a result, a nearly zero-energy Andreev bound state appears within the gap along the $M - \Gamma$ line.

Figure S1(e) shows the surface DOS for the A_u state. Reflecting the presence of Andreev bound states confined within the gap along the $M - \Gamma$ direction, the DOS exhibits a dome-like structure inside the superconducting gap. Unlike in the B_{3u} state, the Andreev bound states in the A_u state exhibit dispersion along the k_x direction, as evidenced by the surface Dirac cone along the $\Gamma - X$ line, and hence, no sharp peak appears. The broad split peaks indicate the presence of the van Hove singularities along the $M - \Gamma$ direction.

The B_{1u} and B_{2u} states

The B_{1u} state is a fully gapped superconducting state since the cylindrical Fermi surface is opened along the k_z axis. Figure S1(b) shows the quasiparticle energy bands for the B_{1u} state. Unlike the A_u state, it exhibits a perfectly
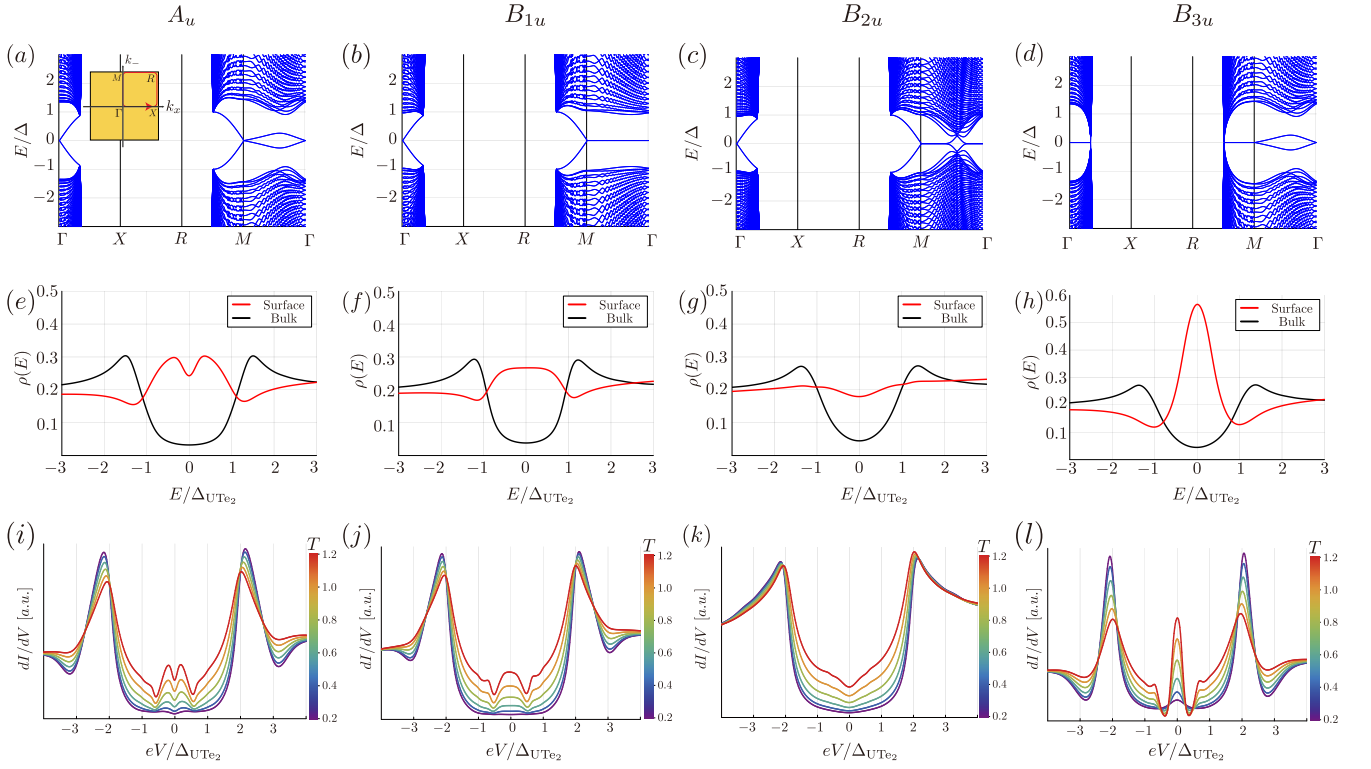
FIG. S1. (a-d) Quasiparticle energy bands for the (a) A_u, (b) B_{1u}, (c) B_{2u}, and (d) B_{3u} states. The inset in (a) shows the path in the surface Brillouin zone along which the bands are plotted. For the A_u state, nearly zero-energy Andreev bound states appear along the $M - \Gamma$ line. A trivial mirror Chern number prevents these states from merging smoothly into the continuum bands. For the B_{1u} and B_{2u} states, zero-energy Andreev flat bands emerge along the $M - \Gamma$ line, protected by one-dimensional (1D) winding number associated with $\mathcal{M}_{yz}$ chiral symmetry. The B_{3u} state hosts both nearly zero-energy Andreev bound states protected by trivial mirror Chern number and zero-energy Andreev flat bands arising from spin conservation, resulting in the formation of an Andreev flatland. (e-h) Density of states (DOS) for the (e) A_u, (f) B_{1u}, (g) B_{2u}, and (h) B_{3u} states. The surface DOS in the A_u, B_{1u}, and B_{2u} states exhibits broad energy dependence in the low-energy regime. In contrast, the surface DOS for the B_{3u} shows a pronounced zero-energy peak. (i-l) Normalized differential conductance (dI/dV) spectra for a point contact between UTe$_2$ and an s-wave superconductor, assuming that the superconducting state of UTe$_2$ is (i) A_u , (j) B_{1u}, (k) B_{2u}, and (l) B_{3u}, respectively. In the calculation, the s-wave superconducting gap is set to $\Delta_s = 2\Delta_{\mathrm{UTe_2}}$. Color bar indicates the tunneling amplitude T.

flat band along the $M - \Gamma$ line. In symmetry class DIII, the only nontrivial topological invariant is the Berry phase at the high-symmetry M and Γ points. Therefore, this flat band must originate from additional topological invariants associated with crystalline symmetries—in particular, the mirror symmetry $\mathcal{M}_{yz}$.

In the following, we describe the topological invariants associated with mirror symmetry [1]. The mirror operator $\mathcal{M}_{yz}$ acts on the normal-state Hamiltonian H_{N} as

$$\mathcal{M}_{yz}^{-1} H_{\mathrm{N}}(k_x, k_+, k_-) \mathcal{M}_{yz} = H_{\mathrm{N}}(-k_x, k_+, k_-), \tag{S1}$$

and on the gap function Δ as

$$\mathcal{M}_{yz}^{-1} \Delta(k_x, k_+, k_-) \mathcal{M}_{yz} = s\Delta(-k_x, k_+, k_-), \tag{S2}$$

where $s = +1$ for the B_{1u} and B_{2u} states, and $s = -1$ for the A_u and B_{3u} states. Depending on the value of s, the mirror operator acting on the Bogoliubov-de Gennes (BdG) Hamiltonian is given by

$$\tilde{\mathcal{M}}_{yz} = \begin{pmatrix} \mathcal{M}_{yz} & \\ & s\mathcal{M}_{yz}^* \end{pmatrix}. \tag{S3}$$

On the mirror plane ($k_x = 0$), this operator $\tilde{\mathcal{M}}_{yz}$ commutes with the BdG Hamiltonian. We can then define a crystalline chiral operator that anti-commutes with the BdG Hamiltonian:

$$\Gamma_{\mathcal{M}_{yz}} = e^{i\phi} \tilde{\mathcal{M}}_{yz} \Theta C, \tag{S4}$$

where $e^{i\phi}$ is a phase factor chosen such that $\Gamma^2_{\mathcal{M}_{yz}} = 1$, Θ is the time-reversal operator, and C is the particle-hole exchange operator. The properties of the chiral operator defined in Eq. (S4) depend on the value of s. For $s = -1$, corresponding to the A_u and B_{3u} states, the chiral operator anti-commutes with the time-reversal operator Θ, which is the same as the standard chiral operator in class DIII, $\Gamma = i\Theta C$. In contrast, for $s = +1$, as in the B_{1u} and B_{2u} states, the chiral operator commutes with the time-reversal operator—characteristic of class BDI. In class BDI, a 1D winding number can be defined using the chiral operator as a topological invariant:

$$w_{\mathcal{M}_{yz}}(k_-) = -\frac{1}{4\pi i} \int dk_+ \ \text{tr} \ [\Gamma_{\mathcal{M}_{yz}} \mathcal{H}_{\text{BdG}} \partial_{k_+} \mathcal{H}_{\text{BdG}}], \tag{S5}$$

where $\mathcal{H}_{\text{BdG}}$ is the BdG Hamiltonian that is composed of H_N and Δ. Note that for the A_u and B_{3u} states, this 1D winding number is not a valid topological invariant, as it always vanishes due to the anti-commutation between the chiral and time-reversal operators.

The winding number in Eq. (S5) can be efficiently calculated using Fermi surface formula. For both the B_{1u} and B_{2u} states, it simplifies to

$$w_{\mathcal{M}_{yz}}(k_-) = \sum_{E_N(k_+)=0} \text{sgn}[d_x]\text{sgn}[\partial_{k_+} E_N], \tag{S6}$$

where $E_N(\boldsymbol{k})$ is the eigenvalue of the normal-state Hamiltonian $H_N(\boldsymbol{k})$. This means that for a fixed k_- on the $k_x = 0$ plane, the winding number can be obtained by summing the products of the signs of the d_x component and the Fermi velocity $\partial_{k_+} E_N$ at each Fermi crossing point along the 1D loop $k_+ \in [-2\pi, 2\pi]$. The resulting winding number is $w = 2$, reflecting the twofold degeneracy of the flat band.

The surface DOS for the B_{1u} state is shown in Fig. S1(f). The Andreev bound states are perfectly flat along the k_- direction, while exhibiting a linear dispersion along the k_x direction [Fig. S1(b)]. As a result, the surface DOS remains constant near zero energy.

The B_{2u} state is qualitatively similar to the B_{1u} state, except for the presence of Dirac points along the $M - \Gamma$ direction [Fig. S1(c)]. Along this line, in addition to the Dirac points, Andreev bound states protected by the 1D winding number also appear. The surface states exhibit a linear dispersion along the k_x direction, resulting in a nearly constant surface DOS with respect to energy, as shown in Fig. S1(g).

S2. ANDREEV CURRENT BETWEEN UTE$_2$ AND s-WAVE SUPERCONDUCTING TIP

In this section, we numerically calculate the tunneling current between a UTe$_2$ sample and an s-wave superconducting tip using Keldysh Green's function formalism. The detailed formulation is provided in the following section. We consider a point-contact junction between UTe$_2$ and an s-wave superconductor. The surface Green's function for the (011) plane of UTe$_2$ is obtained using the recursive Green's function method. The model Hamiltonian for UTe$_2$ is given in the main text and also in Sec. S3. For the s-wave superconductor, we use the analytical expression for the retarded Green's functions:

$$G^R(\omega) = \frac{\pi N_s}{\sqrt{\Delta_s^2 - (\omega + i\delta)^2}} \begin{pmatrix} \omega & \Delta_s \\ \Delta_s & \omega \end{pmatrix}, \tag{S7}$$

where N_s denotes the DOS in the normal state at the Fermi level, and Δ_s is the gap function of the s-wave superconductor. We set the parameters to $\Delta_s = 0.1$ and $N_s = 0.1$. All calculations are performed at zero temperature. Note that in the following calculations, the steady-state tunneling current is independent of the superconducting phase difference, except for the DC Josephson current, which is not considered here.

Figures S1(i)-(l) show the differential conductance (dI/dV) spectra for the A_u, B_{1u}, B_{2u}, and B_{3u} states, respectively, assuming each of these as the superconducting states of UTe$_2$. Here, we calculate the tunneling current using Eq. (S44), taking into account multiple scattering processes between s-wave superconductors and UTe$_2$ via the self-energy given in Eq. (S42). For small tunneling amplitude T, the differential conductance in the low-bias regime $(eV < \Delta_s)$ reflects the surface DOS of the superconducting UTe$_2$ sample . In this regime, the dominant contribution to the tunneling current arises from the Andreev reflection process, in which electrons and holes at the surface of UTe$_2$ are converted into Cooper pairs in the s-wave superconductor, and vice versa. This process corresponds to a fourth perturbative process, and the resulting contribution to the current is given by

$$I^{(4)}(V) = \frac{4e}{\hbar}|T|^4 N_s^2 \pi^3 \int_0^{2eV} dE \ \rho(E - 2eV)\rho(E). \tag{S8}$$
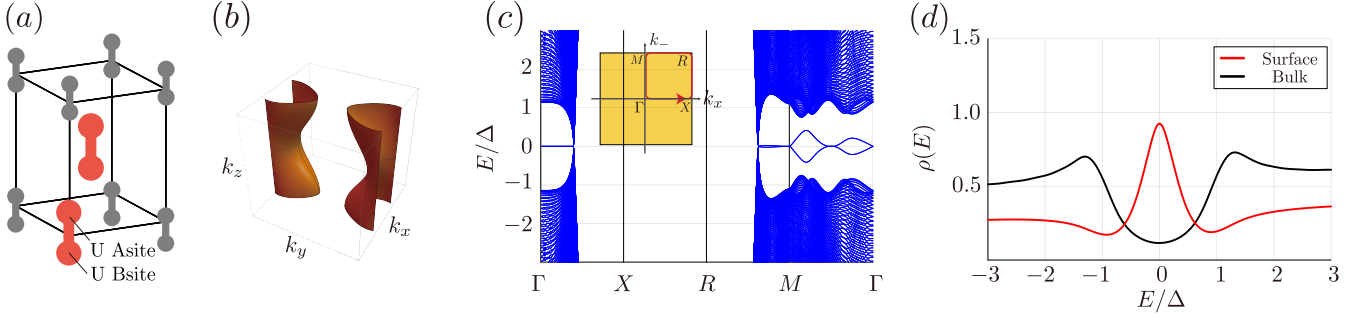
FIG. S2. (a) Crystal structure of UTe$_2$. Only uranium sites are shown. (b) Cylindrical Fermi surface obtained from the two-orbital model. (c) Quasiparticle energy bands for the B_{3u} state in the two-orbital model. The staggered Rashba spin-orbit coupling, originating from local inversion symmetry breaking at uranium sites, has little effect on the zero-energy states. (d) Surface DOS exhibiting a pronounced zero-energy peak due to the presence of robust Andreev flatland.

where $\rho(E)$ is the surface DOS of UTe$_2$. The detailed derivation of this expression is provided in Sec. S4. This expression indicates that, in the weak tunneling regime, the dI/dV spectrum directly reflects the energy dependence of the surface DOS in the superconducting sample UTe$_2$. The low-bias dI/dV spectrum, dominated by the Andreev reflection process, scales as T^4, while the coherence peak around $eV \approx \Delta_{\rm s}$, originating from single particle tunneling, scales as T^2. Therefore, as T increases, the low-bias conductance peaks arising from the Andreev process in Eq. (S8) grow more rapidly than the coherence peak at $eV = \Delta_s$, leading to an anomalous enhancement of the subgap conductance relative to the coherence peak in the dI/dV spectrum [see Figs. S1(i-l)]. Note that unlike in s-wave/s-wave Josephson junctions, where a pronounced coherence peak appears at $eV = \Delta_1 + \Delta_2$, no such total coherence peak is observed in the present case. This is because the surface DOS of the topological superconductor is non-singular and qualitatively different from that of a conventional s-wave superconductor.

S3. TWO-ORBITAL MODEL

In this section, we demonstrate that the Andreev flatland persists even when employing a more realistic model that incorporates key features of UTe$_2$, beyond the simplified model employed in the main text. Figure S2(a) shows the crystal structure of UTe$_2$. UTe$_2$ crystallizes in a body-centered orthorhombic structure with D_{2h} point group symmetry. Within each unit cell, uranium atoms are aligned along the crystal c-axis in a dimer-like configuration, resulting in local inversion symmetry breaking at the uranium sites.

We adopt a two-orbital tight-binding model that includes the site degree of freedom associated with uranium atoms [1, 2]. The normal-state Hamiltonian, which respects the body-centered orthorhombic symmetry, is given by

$$H_{\rm N}(\boldsymbol{k}) = \epsilon_0(\boldsymbol{k}) - \mu + f_x(\boldsymbol{k})\rho_x + f_y(\boldsymbol{k})\rho_y + \boldsymbol{g}(\boldsymbol{k}) \cdot \boldsymbol{\sigma}\rho_z, \tag{S9}$$

where

$$\epsilon_0(\boldsymbol{k}) = 2t_1 \cos k_x + 2t_2 \cos k_y, \tag{S10}$$

$$f_x(\boldsymbol{k}) = t_3 + t_4 \cos(k_x/2)\cos(k_y/2)\cos(k_z/2), \tag{S11}$$

$$f_y(\boldsymbol{k}) = t_5 \cos(k_x/2)\cos(k_y/2)\sin(k_z/2), \tag{S12}$$

$$g_x = R_x \sin k_y, \quad g_y = R_y \sin k_x, \quad g_z = R_z \sin(k_x/2)\sin(k_y/2)\sin(k_z/2). \tag{S13}$$

Here, $\boldsymbol{\sigma}$ and $\boldsymbol{\rho}$ are the Pauli matrices acting on spin and uranium-site spaces, respectively. The last term represents Rashba-type spin-orbit coupling (SOC) arising from local inversion symmetry breaking at the uranium site. To reproduce a cylindrical Fermi surface as shown in Fig. S2(b), we use the following parameters: $\mu = -1.8$, $t_1 = -0.5$, $t_2 = 0.375$, $t_3 = -0.7$, $t_4 = 0.65$, $t_5 = -0.65$, $R_x = 0.1$, $R_y = 0.1$, $R_z = 0.1$.

The gap function also incorporates the site degree of freedom. We consider an inter-site spin-triplet Cooper pair, described by

$$\Delta(\boldsymbol{k}) = \begin{pmatrix} 0 & \boldsymbol{d} \cdot \boldsymbol{\sigma} i\sigma_y \\ \boldsymbol{d} \cdot \boldsymbol{\sigma} i\sigma_y & 0 \end{pmatrix}, \tag{S14}$$

where the matrix structure refers to the uranium-site space. The d-vector for the B_{3u} state is given by $\boldsymbol{d} = \begin{pmatrix} 0 & C_2 \sin k_y & C_3 \sin k_z \end{pmatrix}$, as also used in the main text. We set $C_2 = 0.05$ and $C_3 = 0.05$ in the calculations.

Figure. S2(c) shows the quasiparticle energy bands for the B_{3u} state in the two-uranium-site model, obtained by diagonalizing a slab system with open (011) surfaces. Along the $M - \Gamma$ line, in-gap states appear as a result of nontrivial Berry phases and a trivial mirror Chern number on the yz-mirror plane. Furthermore, even in the presence of staggered Rashba SOC presence, zero-energy states originating from weak spin conservation appear along the $\Gamma - X$ and $R - M$ lines. As a result, the surface exhibits a large zero-energy DOS, as shown in Fig. S2(d).

S4. TUNNELING HAMILTONIAN APPROACH

General expression for the tunneling current by Keldysh Green's function

In this section, we provide a brief derivation of the tunneling current in Josephson junctions using the tunneling Hamiltonian approach [3]. The total Hamiltonian of the system consists of three terms:

$$\mathcal{H} = \mathcal{H}_R + \mathcal{H}_L + \mathcal{H}_T, \tag{S15}$$

$$\mathcal{H}_T = \sum_{k,q} T_{kq} d_k^\dagger c_q + T_{kq}^* c_q^\dagger d_k, \tag{S16}$$

where $\mathcal{H}_{L(R)}$ denotes the Hamiltonian of the left (right) system, constructed from the electron annihilation operators c_q (d_k) and creation operators $c_q^\dagger$ ($d_k^\dagger$). The term $\mathcal{H}_T$ describes the tunneling between the two systems, where T_{kq} is the tunneling matrix element that reflects the geometric structure of the junction. When an STM tip makes contact at a point, the tunnel matrix can be taken as momentum-independent, i.e., $T_{kq} = T$. Although spin degrees of freedom are not explicitly included in the tunneling Hamiltonian, we assume spin-conserving tunneling processes in the absence of SOC and magnetic impurities.

The voltage bias between the two systems can be incorporated as a shift in the chemical potential. Taking the chemical potential of the right system as a reference, the Hamiltonian of the left system under a finite voltage bias V is given by

$$\mathcal{H}_L(V) = \mathcal{H}_L(V = 0) + eV N_L, \tag{S17}$$

where N_L is the total number operator in the left system. In the Heisenberg picture, the operators of the left system transform as

$$\tilde{c}_q(t) = e^{-\frac{i}{\hbar} eV t} c_q(t), \tag{S18}$$

$$\tilde{c}_q^\dagger(t) = e^{\frac{i}{\hbar} eV t} c_q^\dagger(t), \tag{S19}$$

where $c_q(t)$ and $c_q^\dagger(t)$ are the annihilation and creation operators in the Heisenberg picture without the voltage bias.

The tunneling current is defined as the time derivative of the electron number in the left system:

$$I(V, t) = e \langle \dot{N}_L(t) \rangle, \tag{S20}$$

where

$$\begin{aligned} \dot{N}_L &= \frac{i}{\hbar} [\mathcal{H}, N_L] = \frac{i}{\hbar} [\mathcal{H}_T, N_L] \\ &= \frac{i}{\hbar} \sum_{k,q} \left(T_{kq} d_k^\dagger c_q - T_{kq}^* c_q^\dagger d_k \right). \end{aligned} \tag{S21}$$

Here, we used the fact that N_L commutes with both $\mathcal{H}_L$ and $\mathcal{H}_R$. With straightforward manipulation, the tunneling current can be expressed in terms of the lesser Green's function across the junction as

$$I(V, t) = -2e \, \text{Re} \sum_{k,q} \text{tr} \, T(k, q) G_{LR}^<(q, t; k, t'), \tag{S22}$$

where the trace is taken over spin and sublattice degrees of freedom. We now introduce the time-ordered Green's function for the coupled junction system:

$$\hat{G}_{LR} = \begin{pmatrix} G_{LR}^{11} & G_{LR}^< \\ G_{LR}^> & G_{LR}^{22} \end{pmatrix}, \tag{S23}$$

and

$$G_{LR}^{11}(q,t;k,t') = -\frac{i}{\hbar}\langle T_{\rm c}\,\tilde{c}_q(t)d_k^\dagger(t')\rangle, \tag{S24}$$

$$G_{LR}^<(q,t;k,t') = \frac{i}{\hbar}\langle d_k^\dagger(t')\tilde{c}_q(t)\rangle, \tag{S25}$$

$$G_{LR}^>(q,t;k,t') = -\frac{i}{\hbar}\langle \tilde{c}_q(t)d_k^\dagger(t')\rangle, \tag{S26}$$

$$G_{LR}^{22}(q,t;k,t') = -\frac{i}{\hbar}\langle \bar{T}_{\rm c}\,\tilde{c}_q(t)d_k^\dagger(t')\rangle, \tag{S27}$$

where $T_{\rm c}$ ($\bar{T}_{\rm c}$) denotes the contour (anti-contour) time-ordering operator in the Keldysh formalism.

Perturbation theory for the Green's function of the junction

To determine the Green's function of the junction, we treat the tunneling Hamiltonian as a perturbation. For this purpose, it is convenient to introduce the rotated Keldysh basis for perturbation theory:

$$\check{G} \equiv \check{L}\tau_3\hat{G}\check{L}^\dagger = \begin{pmatrix} G^R & G^K \\ 0 & G^A \end{pmatrix}, \quad \check{L} = \frac{1}{\sqrt{2}}(\tau_0 - i\tau_2), \tag{S28}$$

where $\boldsymbol{\tau}$ is the Pauli matrix acting of Keldysh space. G^R, G^A, and G^K denote retarded, advanced, and Keldysh components of Green's function, respectively:

$$G^R(1,2) = G^{11}(1,2) - G^<(1,2) = G^{21}(1,2) - G^{22}(1,2) = -\frac{i}{\hbar}\langle\{c(1),c^\dagger(2)\}\rangle\theta(t_1 - t_2), \tag{S29}$$

$$G^A(1,2) = G^{11}(1,2) - G^>(1,2) = G^{12}(1,2) - G^{22}(1,2) = \frac{i}{\hbar}\langle\{c(1),c^\dagger(2)\}\rangle\theta(t_2 - t_1), \tag{S30}$$

$$G^K(1,2) = G^<(1,2) + G^>(1,2) = G^{11}(1,2) + G^{22}(1,2) = -\frac{i}{\hbar}\langle[c(1),c^\dagger(2)]\rangle, \tag{S31}$$

where we used the shorthand notation $(1) = (q,t)$ and $(2) = (k,t')$. In thermal equilibrium at inverse temperature β, the Keldysh component takes the form

$$G^K(q,\omega) = (G^R(q,\omega) - G^A(q,\omega))\tanh\frac{\beta\omega}{2}. \tag{S32}$$

Full Green's functions are governed by the Dyson equation, in which the tunneling matrix acts as an effective single-particle potential:

$$\begin{bmatrix} \check{G}_{LL} & \check{G}_{LR} \\ \check{G}_{RL} & \check{G}_{RR} \end{bmatrix} = \begin{bmatrix} \check{G}_{LL}^{(0)} & \\ & \check{G}_{RR}^{(0)} \end{bmatrix} + \begin{bmatrix} \check{G}_{LL}^{(0)} & \\ & \check{G}_{RR}^{(0)} \end{bmatrix} \circ \begin{bmatrix} & \check{T} \\ \check{T}^\dagger & \end{bmatrix} \circ \begin{bmatrix} \check{G}_{LL} & \check{G}_{LR} \\ \check{G}_{RL} & \check{G}_{RR} \end{bmatrix}. \tag{S33}$$

Here, $\check{G}_{LL}$, $\check{G}_{RR}$, and $\check{G}_{RL}$ are defined analogously to $\check{G}_{LR}$ in Eqs. S24-S27. The quantities $\check{G}_{LL}^{(0)}$ and $\check{G}_{RR}^{(0)}$ correspond to the Green's functions of $\mathcal{H}_L$ and $\mathcal{H}_R$, respectively. In the rotated Keldysh space, the tunneling matrix is given by

$$\check{T} = \delta(t - t')\begin{pmatrix} T_{kq} & \\ & T_{kq} \end{pmatrix}. \tag{S34}$$

The circle product "$\circ$" denotes integration over the internal variables:

$$[\check{G} \circ \check{T} \circ \check{G}](1,4) \equiv \sum_{k_2,k_3}\int dt_2 dt_3\,\check{G}(1,2)\check{T}(2,3)\check{G}(3,4). \tag{S35}$$

By solving for $\check{G}_{LR}$, we obtain

$$\begin{aligned} \check{G}_{LR} &= \check{G}_{LL}^{(0)} \circ \check{T}^\dagger \circ \check{G}_{RR}^{(0)} + \check{G}_{LL}^{(0)} \circ \check{T}^\dagger \circ \check{G}_{RR}^{(0)} \circ \check{T} \circ \check{G}_{LR} \\ &= \check{G}_{LL}^{(0)} \circ \check{\Sigma} \circ \check{G}_{RR}^{(0)}, \end{aligned} \tag{S36}$$

where we have introduced a self-energy $\check{\Sigma}$, satisfying a following Dyson equation

$$\check{\Sigma} = \check{T}^\dagger + \check{T}^\dagger \circ \check{G}_{RR}^{(0)} \circ \check{T} \circ \check{G}_{LL}^{(0)} \circ \check{\Sigma}. \tag{S37}$$

Solving the Dyson equation for the self-energy yields the full Green's function across the junction.

Fourier representations

To solve the Dyson equations, we introduce Fourier representations. In the right system, the Green's function depends only on the relative time $t - t'$, and its Fourier transform is given by

$$\check{G}_{RR}^{(0)}(t,t') = \int \frac{d\omega}{2\pi} \, e^{-i\omega(t-t')} \check{G}_{RR}^{(0)}(\omega). \tag{S38}$$

In contrast, in the superconducting case, Green's function in the left system explicitly depends on both t and t' due to the gauge potential induced by the voltage. It takes the following form

$$\check{G}_{LL}^{(0)}(t,t') = \begin{pmatrix} e^{-\frac{i}{\hbar}eV(t-t')} \check{g}_L(t-t') & e^{-\frac{i}{\hbar}eV(t+t')} \check{f}_L(t-t') \\ e^{\frac{i}{\hbar}eV(t+t')} \check{f}_L^\dagger(t-t') & e^{\frac{i}{\hbar}eV(t-t')} \check{g}_L^\dagger(t-t') \end{pmatrix}, \tag{S39}$$

where $\check{g}$ and $\check{g}^\dagger$ denote the normal Green's functions for particles and holes, respectively, and $\check{f}$ and $\check{f}^\dagger$ represent the anomalous Green's functions. Note that in the normal state, where anomalous components vanish, Green's function depends only on the relative time, and thus a standard Fourier transform applies. To handle the time dependence in the superconducting case, we introduce a discrete frequency component $\Omega_n = 2eVm/\hbar$, and perform a mixed Fourier transform:

$$\check{G}_{LL}^{(0)}(t,t') = \int \frac{d\omega}{2\pi} \sum_n e^{-i\omega(t-t')} e^{-i\Omega_n t} \check{G}_{LL}^{(0)}(\omega, \Omega_n) \tag{S40}$$

$$\check{G}_{LL}^{(0)}(\omega, \Omega_n) = \begin{pmatrix} \delta_{n,0} \, \check{g}_L(\omega - eV/\hbar) & \delta_{n,1} \, \check{f}_L(\omega + eV/\hbar) \\ \delta_{n,-1} \, \check{f}_L^\dagger(\omega - eV/\hbar) & \delta_{n,0} \, \check{g}_L^\dagger(\omega + eV/\hbar) \end{pmatrix}, \tag{S41}$$

where $\delta_{i,j}$ is the Kronecker delta. Applying the same transformation to the self-energy, the Dyson equation becomes

$$\check{\Sigma}(\omega, \Omega_n) = \delta_{n,0}\check{T}^\dagger + \check{T}^\dagger \circ \check{G}_{RR}^{(0)}(\omega + \Omega_n) \circ \check{T} \circ \sum_{n'} \check{G}_{LL}^{(0)}(\omega + \Omega_n', \Omega_n - \Omega_n') \circ \check{\Sigma}(\omega, \Omega_n'), \tag{S42}$$

where the circle product implies summation over the momentum variables. Substituting this into the expression for the Green's function at equal time, we obtain

$$\check{G}_{LR}(t,t) = \sum_n e^{-i\Omega_n t} \int \frac{d\omega}{2\pi} \sum_{n'} \check{G}_{LL}^{(0)}(\omega + \Omega_n', \Omega_n - \Omega_n') \circ \check{\Sigma}(\omega, \Omega_n') \circ \check{G}_{RR}^{(0)}(\omega). \tag{S43}$$

The steady tunneling current arises from the $\Omega_n = 0$ components.

When the junction is formed by a point contact, as in STM experiments, the tunneling matrix becomes momentum-independent, simplifying the expression for the tunneling current:

$$I(V,t) = -2e|T|\,\mathrm{Re}\,\mathrm{tr}\,\langle G_{LR}^<(t,t)\rangle_{k,q}, \tag{S44}$$

where momentum-summed Green's function is defined as $\langle G_{LR}^<(t,t')\rangle_{k,q} = \sum_{k,q} G_{LR}^<(k,t;q,t')$. The Dyson equation governing the momentum-summed Green's function then takes the form

$$\langle \check{G}^{LR}(t,t')\rangle_{k,q} = \sum_n e^{-i\Omega_n t} \int \frac{d\omega}{2\pi} \sum_{n'} \langle \check{G}_{LL}^{(0)}(\omega + \Omega_n', \Omega_n - \Omega_n')\rangle_k \langle \Sigma(\omega, \Omega')\rangle_{k,q} \langle \check{G}_{RR}^{(0)}(\omega)\rangle_q, \tag{S45}$$

where the self-energy satisfies

$$\langle \check{\Sigma}(\omega, \Omega_n)\rangle_{k,q} = |T|\delta_{n,0} + |T|^2 \langle \check{G}_{RR}^{(0)}(\omega + \Omega_n)\rangle_q \sum_{n'} \langle \check{G}_{LL}^{(0)}(\omega + \Omega_n', \Omega_n - \Omega_n')\rangle_k \langle \Sigma(\omega, \Omega_n')\rangle_{k,q}. \tag{S46}$$

Here, we define $\langle \check{G}_{LL}^{(0)}(\omega, \Omega_n)\rangle_k = \sum_k \check{G}_{LL}^{(0)}(k,\omega, \Omega_n)$ and $\langle \check{G}_{RR}^{(0)}(\omega, \Omega_n)\rangle_q = \sum_q \check{G}_{LL}^{(0)}(q,\omega)$.
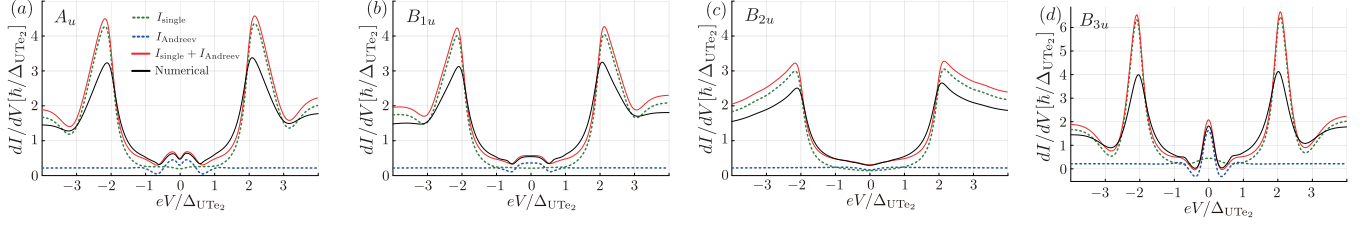
FIG. S3. Comparison between numerical calculations and analytical expressions. The tunneling amplitude is set to $T = 0.8$. The black solid curves represent numerically calculated dI/dV spectra, incorporating tunneling processes to all orders in perturbation theory. The dotted green curves correspond to the analytical result of single-particle tunneling [Eq. S48]. The dotted blue curves correspond to the analytical result of Andreev tunneling current [Eq. S53]. The red curves correspond to the sum of the contributions from Eq. S48 and Eq. S53. In the low-bias regime, the dI/dV characteristics are governed by the Andreev tunneling current. In contrast, in the high-bias regime ($eV > \Delta_s$), the single-particle tunneling contribution becomes dominant.

Andreev current for a point contact between a topological superconductor and an s-wave superconductor

We consider a point-contact junction in which a topological superconductor is placed on the right side and an s-wave superconductor on the left side. For notation simplicity, we denote the momentum-summed Green's function as $G(\omega)$ throughout the following discussion. Expanding Eq. S44 to second order in the tunneling matrix element T, the tunneling current is given by

$$I^{(2)}(V,t) = -2|T|^2 e \operatorname{Re} \operatorname{tr} \int \frac{d\omega}{2\pi} \left\{ [\check{g}_L(\omega - eV/\hbar)\check{g}_R(\omega)]^< - e^{-2ieVt/\hbar}[\check{f}_L(\omega + eV/\hbar)\check{f}_R^\dagger]^< \right\}. \tag{S47}$$

The first term represents the single particle tunneling contribution I_{single}. By straightforward calculation, we obtain a familiar form

$$I_{\text{single}} = (4\pi T^2 e/\hbar) \int_0^{eV} dE\ \rho_{\text{tip}}(E - eV)\rho_{\text{sample}}(\omega), \tag{S48}$$

where ρ_{tip} and ρ_{sample} correspond to the DOS for the left and right systems, respectively. Here, we have used spectrum representation of the retarded/advanced Green's function

$$g^{R/A}(\omega) = \int dE\ \frac{\rho(E)}{\hbar\omega \pm i\delta - E}, \tag{S49}$$

$$g^{\dagger R/A}(\omega) = \int dE\ \frac{\rho(E)}{\hbar\omega \pm i\delta + E}. \tag{S50}$$

However, since an s-wave superconducting tip has no quasiparticle states within the superconducting gap, this contribution vanishes. The second term in Eq. S47 corresponds to the Josephson current. In this case, since the junction is formed between a spin-triplet and a spin-singlet superconductor, the orthogonality in spin space leads to the vanishing of this term as well. Note, however, that if SOC coupling or magnetic impurities are present, a finite Josephson current may be induced, although it is generally expected to be small.

The leading contribution to the steady tunneling current thus arises from fourth-order tunneling processes. The dominant contribution is Andreev tunneling current, which originates from Andreev reflection and is given by

$$I_{\text{Andreev}} = -4e|T|^4 \operatorname{Re} \int \frac{d\omega}{2\pi} [\check{f}_L(\omega)\check{g}_R^\dagger(\omega - eV/\hbar)\check{f}_L^\dagger(\omega)\check{g}_R(\omega + eV/\hbar)]^<. \tag{S51}$$

In this process, electrons and holes in the topological superconductor are converted into Cooper pairs in the s-wave superconductor and vice versa through tunneling. We employ the analytical expression for the anomalous Green's function of the s-wave superconductor:

$$f_L^{R/A}(\omega) = f_L^{\dagger R/A}(\omega) = -\frac{N_L \pi \Delta_s}{\sqrt{\Delta^2 - (\hbar\omega \pm i\delta)^2}}, \tag{S52}$$

where N_L denotes DOS at the Fermi level, and Δ_s is the superconducting gap amplitude. By straightforward calculation, we obtain the final expression:

$$I_{\text{Andreev}}(V) = (4e\pi^3|T|^4 N_L^2/\hbar) \int_0^{2eV} dE \; \rho_{\text{sample}}(E - 2eV)\rho_{\text{sample}}(E). \tag{S53}$$

It is noteworthy that the Andreev current is independent of the superconducting gap Δ_s.

Figure S3 compares the numerical calculations with the analytical expressions. The black solid curves represent the numerically computed dI/dV spectra, incorporating tunneling processes to all orders in perturbation theory. The red curves correspond to the analytical results, which are the sum of contributions from single-particle tunneling current [Eq. S48], shown by green dotted lines, and Andreev tunneling current [Eq. S53], shown by blue dotted lines. Note that, due to the presence of a small but finite smearing factor, single-particle tunneling contributes even within the gap of the s-wave superconductor. In the low-bias regime, the analytical expressions agree well with the numerical results. Moreover, the peak structure at low bias is predominantly governed by Andreev tunneling current. When the DOS is large and the tunneling probability is high, higher-order processes can act as self-energy corrections that suppress the tunneling current. As a result, the coherence peaks of the s-wave superconductor, which appear at $eV = 2\Delta_{\text{UTe}_2}$, are more suppressed in the numerical results than in the analytical results, which only account for contributions up to the fourth order. Similarly, the zero-bias peak for the B_{3u} state [Fig. S3(d)] also exhibits suppression in the numerical calculation.

---

* tei@blade.mp.es.osaka-u.ac.jp

[1] J. Tei, T. Mizushima, and S. Fujimoto, Possible realization of topological crystalline superconductivity with time-reversal symmetry in UTe$_2$, Phys. Rev. B **107**, 144517 (2023).

[2] T. Shishidou, H. G. Suh, P. M. R. Brydon, M. Weinert, and D. F. Agterberg, Topological band and superconductivity in UTe$_2$, Phys. Rev. B **103**, 104504 (2021).

[3] J. C. Cuevas, A. Martín-Rodero, and A. L. Yeyati, Hamiltonian approach to the transport properties of superconducting quantum point contacts, Phys. Rev. B **54**, 7366 (1996).